Wear reduction mechanisms in modulated turning of compacted graphite iron with coated carbide tool

Juan Sandoval [a], Aaqib Ali [a], Patrick Kwon [a], David Stephenson [b], Yang Guo [a1]
[a] Department of Mechanical Engineering, Michigan State University, East Lansing, MI 48824, USA
[b] Ford Motor Company, Livonia, MI 48150, USA
[1]Corresponding author; email: yguo@msu.edu

Abstract

Tool wear evolution is characterized in detail for turning compacted graphite iron (CGI) with coated carbide tool under conventional machining (CM) and modulation-assisted machining (MAM) in dry and lubricated conditions at a speed of 250 m/min. Significant wear reductions are achieved by MAM compared to CM turning. MAM dry turning leads to lower tool wear than MAM lubricated turning. It is found that two wear phenomena account for the wear reduction in MAM: 1) the formation of SiO_2 deposition layer on tool flank and 2) the preservation of the coatings on the cutting edge. The mechanisms on how the wear progression is slowed down by the observed wear phenomena as well as these phenomena are enabled by MAM are discussed.

Keywords: machining, wear, abrasive, adhesive

1. Introduction

Compacted graphite iron (CGI) has long been considered as a next generation material to replace gray cast iron or flake graphite iron (FGI) for making diesel engine blocks and heads [1]. Due to its excellent mechanical properties, engine block made of CGI can be lighter and withstand higher combustion pressure and temperature which will increase the fuel economy and reduce emission. However, the capital investment for CGI components is roughly one third higher than for FGI components due to the reduced cutting speeds [2]. For example, FGI can be machined at high speeds (~800 m/min) with cubic boron nitride (CBN) tools, but CBN cannot be used for machining CGI at such high speed because of rapid tool wear. It has been shown that CBN tool life when machining CGI is only $1/20^{th}$ of that when machining FGI [3,4]. Therefore, CGI is often machined at lower speeds (~ 100 m/min) with coated carbide tools. When machining CGI at speeds beyond 200 m/min, the coated carbide tool life is significantly reduced and is often several folds lower than that when machining FGI [3,5].

The reason that CBN tools work exceptionally well for cutting FGI at extremely high speeds (~800 m/min) has been attributed to the formation of MnS layer on the tool face which acts as a lubricant and also protects the tool from diffusion and dissolution [6,7]. Such MnS layer is not formed during cutting CGI because the sulfur content in CGI is significantly lower than in FGI owing to the process of creating vermicular shaped graphite. Alternately, the drastic difference in CBN tool life between cutting FGI and CGI is explained by the formation of protective Al_2O_3 layer on the tool face [8]. The manganese present in FGI acting as a sintering agent help the aluminum or alumina present in the binder of CBN tool to consolidate into a stable Al_2O_3 layer on the tool face during cutting. Because the manganese content is low in CGI, the Al_2O_3 layer formed during cutting CGI is not as stable as that formed during cutting FGI.

Without the protective layer formation (either MnS or stable Al_2O_3), CGI will react with the binder phase of CBN tool at such high cutting speeds leading to rapid chemical wear and hence significantly reduced tool life.

The reduced carbide tool life in cutting CGI compared to FGI at lower cutting speeds has been attributed to the increased abrasive and adhesive wear during cutting CGI [9]. Due to different graphite morphology, CGI has higher fracture toughness compared to FGI [10]. This leads to increased plastic deformation, larger tool-chip contact and hence higher cutting temperature when machining CGI [11,12]. The hot hardness of the tool and coating material is critical for resisting the abrasive wear in cutting CGI. Earlier study on cutting CGI with multi-layer (TiCN/ Al_2O_3/TiN) coated carbides showed that TiCN coating layer is more effective in resisting flank wear than the Al_2O_3 and TiN coating layers [5]. This is consistent with the fact that TiCN has higher hot hardness compared to Al_2O_3 and TiN. Nonetheless, the tool life for the multi-layer coated carbides is still significantly lower for cutting CGI compared to FGI. Moreover, there is a higher tendency to form built-up edge (BUE) or dead metal zone near the tool cutting edge when cutting CGI. It has been observed that BUE formation occurs for FGI only in a narrow range of cutting speeds while it occurs for the more ductile CGI in a much wider range of cutting speeds [13]. The formed BUE or dead metal is usually not stable, frequently detaching and reappearing in the cutting process, which is detrimental to the tool cutting edge. Indeed, edge chipping is often observed when machining CGI with coated carbide tools [5].

The poor machinability of CGI may be addressed by using process enhancement techniques. For example, the application of cutting fluid can be considered as the most used process enhancement technique. It provides the lubrication effect mainly for lower cutting speeds

and the cooling effect mainly for higher cutting speeds [14]. While FGI can be machined in dry condition, CGI will require the application of cutting fluids especially in continuous cutting operation [15]. For cost and environmental reasons, it is always desired to minimize or eliminate the use of cutting fluid whenever possible [16]. Laser heating can be also used to enhance the cutting process. The main effect comes from softening the work materials before entering the shear zone to reduce the cutting force [17]. It was shown that laser-assisted machining (LAM) of CGI increases tool life by 60% compared to conventional machining at a low cutting speed (100 m/min) with uncoated carbide inserts [18]. However, the benefits of laser heating are likely limited to only low cutting speeds. The required laser power to induce the same softening effect will increase proportionally with the cutting speed, which makes the process unsustainable in improving the productivity. Moreover, at higher cutting speeds, the increase in the cutting temperature accelerates tool wear as the wear mechanism is more dominated by diffusion/dissolution.

Tool vibration is another type of process enhancement technique where the benefits come from the periodic tool-chip or tool-work disengagements (intermittent cutting). The vibration can be applied either in the cutting velocity direction or in the tool feed direction. For the velocity-direction vibration, the tool-chip disengagements are realized when the vibration velocity is higher than the cutting velocity. This condition can be achieved using ultrasonic vibration frequency but only for low cutting speeds [19,20]. This type of ultrasonic vibration assisted cutting (UVAC) has been successfully used for ultra-precision machining of difficult-to-cut materials [21], but it cannot be used for the common machining applications due to the limitation on the cutting speed. For the feed-direction vibration, the tool-work disengagements are realized when the vibration amplitude is higher enough compared to the tool feed rate for the selected

vibration frequency (see details in section 2). The realization of this condition is not dependent on the cutting speed. Both ultrasonic vibration and low-frequency vibration can be used to achieve this condition [22,23]. However, ultrasonic vibration usually has a very small amplitude which limits the applicable feed rate. Therefore, low-frequency feed-direction vibration is more suitable for both practical cutting speeds and feed rates. The application of this type of vibration in machining is referred to as modulation-assisted machining (MAM) [22].

It was shown that turning CGI under MAM with CBN tools increased the tool life by at least 20 times compared to conventional turning when the cutting speed was between 550 and 750 m/min [24]. Dry turning CGI under MAM with coated carbide tools also increased the tool life by multiple times compared to conventional turning when the cutting speed was between 250 and 350 m/min [25]. While these earlier studies clearly demonstrated the effectiveness of MAM for improving the machinability of CGI, the mechanisms on how MAM leads to the significant tool wear reduction during cutting CGI with specific tool material have not been investigated and fully understood. The present study is focused on understanding the mechanisms behind the machinability improvement when tuning CGI under MAM with coated carbide tools. Tool wear evolution is characterized in detail after turning CGI under conventional machining (CM) and MAM in dry and lubricated conditions at the cutting speed of 250 m/min. It shows significant wear reductions are achieved by MAM turning compared to CM turning. Moreover, MAM dry turning leads to more wear reduction than MAM lubricated turning. It was found that two wear phenomena account for the wear reduction in MAM: 1) the formation of SiO_2 deposition layer on the tool flank and 2) the preservation of the coatings on the cutting edge. The exact mechanisms on how the wear progression is slowed down by the observed wear phenomena as well as these phenomena are enabled by MAM are discussed. Although this study is limited to

cutting CGI, the mechanisms observed in MAM may be applicable in improving the machinability of other difficult-to-cut materials.

2. Modulation-assisted Machining

Modulation-assisted machining is a novel machining process in which a controlled low-frequency (< 500 Hz) tool vibration is superimposed onto the tool feed motion during cutting, such that a continuous cutting process, e.g., turning, boring, and drilling, can be divided into a series of discrete cutting events [22,26]. The benefits of MAM include better chip management [27], improved cutting fluid penetration [28], and reduced chip deformation [29]. Figure 1 illustrates the MAM turning process. In conventional machining (CM) turning (Fig. 1a), the constant feed rate generates a parallel helical tool path on the revolving workpiece surface. The tool is always engaged with the workpiece leading to continuous cutting. The uncut chip thickness always stays constant. In contrast, when a properly controlled tool vibration is applied in the tool feed direction (Fig. 1b), the resultant feed rate becomes modulated which generates a sinusoidal wave tool path on the revolving workpiece surface. When the wave tool path is out of

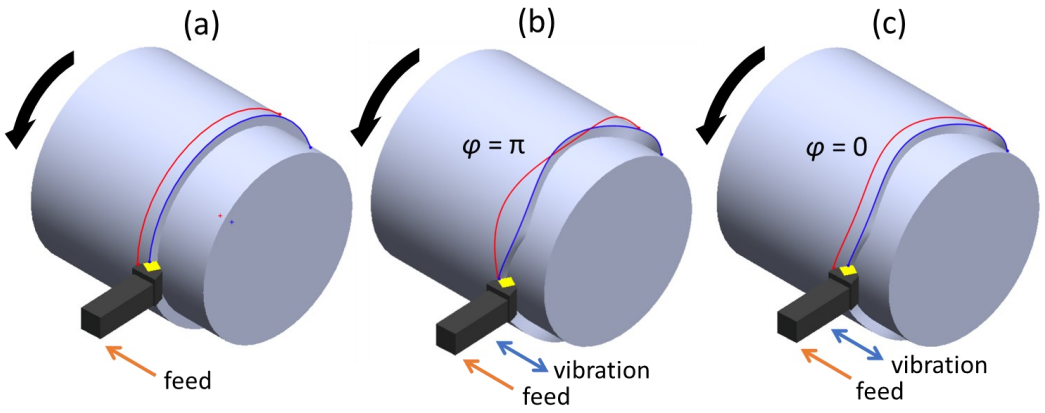

Figure 1. Schematic of (a) CM turning, (b) MAM turning with phase of π, and (c) MAM turning with phase of 0 or 2π.

phase among successive revolutions and the wave amplitude is high enough, the tool path then intercepts between successive revolutions. This means the tool is periodically disengaged from the workpiece leading to a discrete cutting process. The wave tool path shown in Fig. 1b has the phase of $\varphi = \pi$. The vibration frequency and amplitude required to achieve tool path interception or discrete cutting at $\varphi = \pi$ are [22]

$$f_m / f_w = (2N+1)/2, \quad N=0,1,2, \cdots \quad (1)$$

$$A \geq h_0/2 \quad (2)$$

where f_m is the vibration frequency, f_w is the workpiece rotation frequency (=RPM/60), A is the vibration amplitude, and h_0 is the tool feed per revolution. Equation (1) is the condition for generating wave tool path with the phase $\varphi = \pi$. It states that the ratio of vibration frequency to rotation frequency should be equal to half integer values, i.e., 0.5, 1.5, 2.5, 3.5, etc. Equation (2) states the amplitude threshold for discrete cutting is at the half of the feed per revolution (or peak-to-peak amplitude ($2A$) threshold is the feed per revolution). The amplitude threshold corresponding to $\varphi = \pi$ is the smallest amplitude threshold. Other φ values will lead to higher amplitude thresholds for achieving discrete cutting. At the extreme, discrete cutting is not possible with the phase $\varphi = 0$ or 2π (in phase) because the wave tool path becomes always parallel between successive revolutions (Fig. 1c). Therefore, $\varphi = \pi$ (out of phase) is often the preferred phase condition to apply MAM.

3. Materials and Methods

Figure 2 shows the MAM turning setup used in this study. The setup is implemented on a Haas TL-1 toolroom lathe. The tool vibration device consists of a stationary frame (1), two linear guides (2), a moving stage (3), and a piezo stack actuator (4). The tool holder is fixed to the

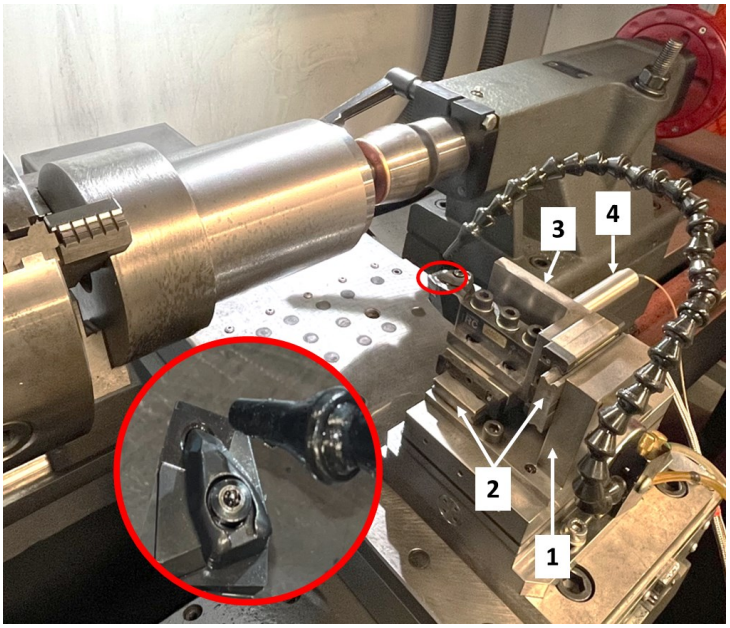

Figure 2. MAM turning setup

moving stage supported by two linear guides. The rails of the linear guides are fixed to the stationary frame. The linear guides constrain the tool motion to only in the tool feed direction. Tool vibration is generated by the piezo stack actuator. The casing of the actuator is fixed to the stationary frame and its actuating head is connected to the moving stage. The piezo stack actuator has a nominal stroke of 0.1 mm, which can generate a maximum driving force of 4000 N. The frequency and amplitude of the tool vibration are controlled by a sinusoidal voltage input to the actuator. The driving voltage is provided by a waveform generator (BK4007B) and a power amplifier (MMech PX200). To measure cutting forces, the tool vibration device is mounted onto a Kistler dynamometer plate (9257B) which is fixed onto the carriage of the lathe. The force signal is recorded using a data acquisition system with a sampling rate of 5000/s and processed with a low-pass filter with a cutoff frequency at 500 Hz.

The CGI workpieces (SinterCast AB) has a hollow cylinder shape with an outer diameter of 145 mm and inner diameter of 98 mm, and a length of 204 mm. The grade is GJV-450 by ISO

standard 16112:2017 with a tensile strength of 450 MPa. The iron matrix is mainly pearlite (95%). The cutting inserts are multi-layer coated carbides (Sandvik Coromant SNMA 12 04 08-KR 3205), with a two-layer coating (TiCN / Al_2O_3) on the rake face and three-layer coating (TiCN / Al_2O_3 / TiN) on the flank face. The toolholder is Sandvik DSBNR 2020K. When used together, it results in a side cutting edge angle of 15° and a rake angle of -6°. For lubricated cutting, the applied cutting fluid is Coolube 2210 (UNIST) which consists of pure vegetable oil recommended for minimum quantity lubrication (MQL) machining ferrous materials. The fluid is delivered to the cutting zone as continuous stream at a flow rate of 1.7 ml/s through a nozzle placed above the tool rake face.

Table 1 lists all the turning tests reported in this study. Each test is performed with a new tool. The cutting speed (V_c = 250 m/min), feed rate (h_o = 0.04 mm/rev) and the depth of cut (d = 1.5 mm) are kept the same for all tests. The main controlled variables are the tool modulation condition (CM vs. MAM) and the cutting fluid condition (dry vs. lubricated). For MAM turning, the frequency ratio is set to f_m/f_w = 9.5, so the wave tool path has a phase of $\varphi = \pi$ (see Fig. 1b) and the tool disengages from the workpiece 9.5 times per revolution. Since the rotation

Table 1. The list of turning tests reported in this study.

Tool number	Turning condition	Total cutting distance
1	CM-dry	3.6 km
2	CM-lubricated	4.8 km
3	MAM-dry	7.2 km
4	MAM-lubricated	7.2 km
5	CM-dry	2.4 km
6	CM-lubricated	2.4 km
7	MAM-dry	2.4 km
8	MAM-lubricated	2.4 km
9	MAM-dry	3.6 km
10	MAM-dry	5.0 km

frequency (f_w) varies with the diameter of the workpiece to maintain a constant cutting speed, the vibration frequency (f_m) will also be varied accordingly (within 90 – 112 Hz) to maintain the constant frequency ratio. The driving voltage peak-to-peak amplitude is set to V_{pp} = 150 V which results in a peak-to-peak tool vibration amplitude (A_{pp} = 2A) of ~90 μm without loading. The vibration amplitude during cutting will be reduced due to the elastic deformation of the vibration device assembly under the variable loading. The amplitude reduction can be calculated as $\Delta A_{pp} = (F_{max} - F_{min})/K$ where K is the stiffness of the vibration device assembly (~12 N/μm measured for the current device) and F_{max} and F_{min} are the maximum and minimum feed force during MAM turning. Based on the measured forces, the actual amplitude A_{pp} of tool vibration during MAM turning is in the range of 55 – 65 μm which is sufficient to enable tool-work separation based on Eq. (2).

To measure tool wear, each turning test is consisted of several cutting intervals. For most cases, each cutting interval has 1.2 km cutting length. After each cutting interval, the tool is cleaned with ethanol in an ultrasonic cleaner. Tool wear is then observed and measured using a Nikon eclipse LV100ND microscope and / or a Keyence VHX6000 digital microscope. Then, the test is resumed with the same tool for the next cutting interval. At the final cutting distance, the tool is characterized more comprehensively before and after etching with HCL (19%) for 45 minutes to remove adhesion. The 3D topography and 2D section profiles of the wear land are measured using Keyence VHX6000 digital microscope at high resolutions. The compositions of the materials present at the wear land are measured using a JEOL 6610LV scanning electron microscope (SEM) equipped with energy dispersive spectroscopy (EDS).

4. Results and Discussion

4.1. General observation on tool wear and forces

Figure 3 shows the optical images of the tool main flank face after every cutting interval (1.2 km) for each turning condition. The progression of the flank wear (VB_{max}) with the cutting distance measured based on these images is shown in Figure 4. It is evident that the progression of flank wear is significantly slower in MAM than CM regardless of the lubrication condition. In CM turning, the flank wear starts to progress rapidly after cutting only a short distance which is evidenced by the sharp upturn of the wear curve at 2.4 km cutting distance for the CM-dry case

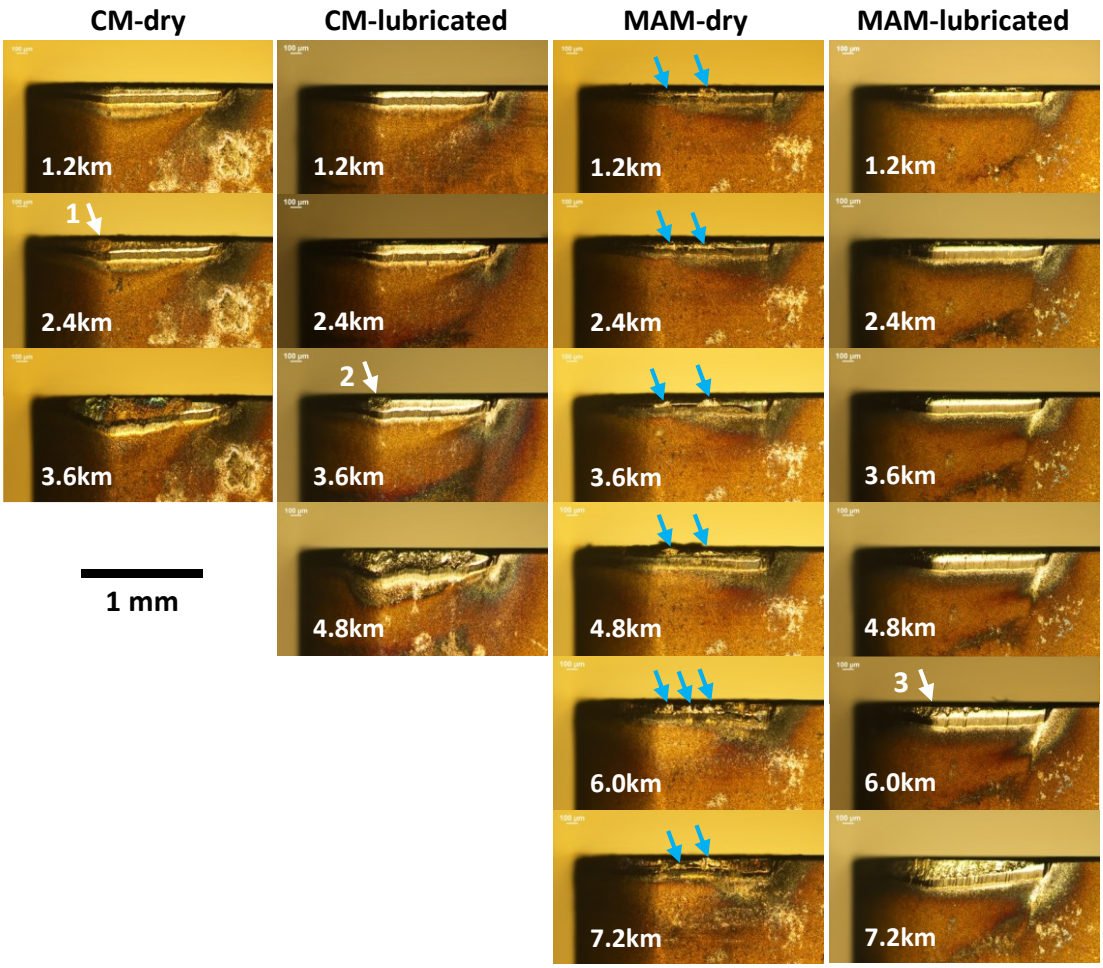

Figure 3. Optical images of tool flank wear after every cutting interval (1.2 km) for each turning condition. Tool number: 1, 2, 3 and 4.

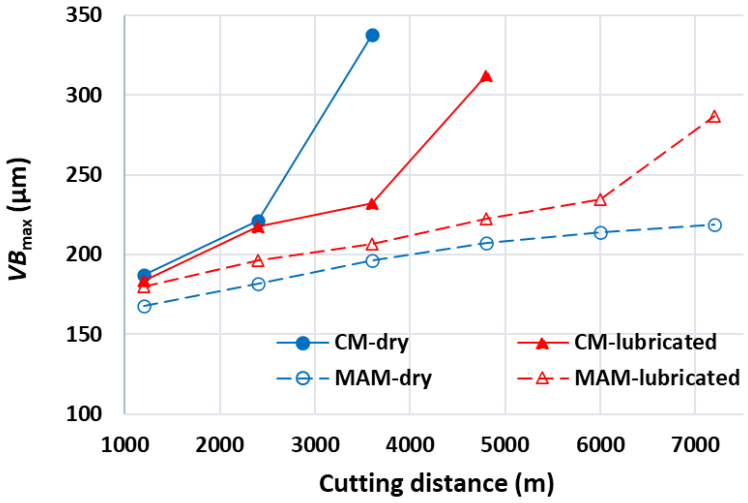

Figure 4. The progression of VB_{max} with cutting distance for different turning conditions

and 3.6 km cutting distance for the CM-lubricated case (Fig. 4). The rapid wear progression is accompanied by the occurrence of severe adhesion on the tool for both CM cases (see arrows 1 and 2 in Fig. 3). It appears that the application of cutting oil reduces tool wear in CM turning by delaying the start of the rapid wear progression associated with severe adhesion. However, the cutting oil seems to have no effect in mitigating the severe adhesion once it has started, and hence no effect in slowing the rapid wear progression. Once the rapid wear progression starts, the flank wear quickly increases beyond 300 µm which is commonly used as the criterion for the end of tool life.

In contrast to CM turning, the progression of flank wear in MAM turning remains steady at a low wear rate up to a much longer cutting distance. For MAM-lubricated case, a noticeable increase in the wear rate occurs after the cutting distance reaches 6 km (Fig. 4). This is again accompanied by the occurrence of severe adhesion (see arrow 3 in Fig. 3). Surprisingly, the MAM-dry case results in the lowest wear. The wear curve for MAM-lubricated case is always above the curve for MAM-dry case which even has a slight decrease in wear rate toward the end

of the curve. At 7.2 km cutting distance, the measured VB_{max} is 219 and 287 μm for MAM-dry and MAM-lubricated case, respectively. The wear in MAM-lubricated case is about 30% higher than the wear in MAM-dry case.

The adhesion occurred in MAM-dry case is unique (see Fig. 3). For other three cases, the initiation of severe tool adhesion can be clearly identified at some cutting distance (see arrows 1, 2 and 3 in Fig. 3), and the wear progression can be divided into two distinctive stages: 1) the steady wear without adhesion and 2) the rapid wear accompanied by severe adhesion. For MAM-dry case, tool adhesion starts to occur right from the beginning and increases more gradually throughout the test (see blue arrows in Fig. 3). The adhesion appears to be more loosely attached to the tool and its distribution on the tool is not as continuous as in the other three cases. More importantly, the adhesion in MAM-dry case is not associated with rapid wear progression.

Figure 5 shows the history of the cutting forces during each cutting interval (cutting distance of every 1.2 km) for the four turning cases. The corresponding average forces over each interval are plotted in Figure 6. The changes in forces with increasing cutting distance (or at each cutting interval) should reflect the tool wear or tool adhesion effect. For all cases, the feed force is more sensitive than the cutting force because the wear and adhesion mainly occur on the tool flank face. For both CM-dry and CM-lubricated cases, the rapid increase in forces in the last cutting interval corresponds to the rapid wear and severe adhesion occurring in that interval (see Fig. 3). In MAM, the forces always oscillate due to the tool vibration, so the forces appear as the bands in the history plots (Fig. 5). For MAM-dry case, the forces generally remain steady during each cutting interval, but there is a clear trend that the forces increase steadily from one interval to the next interval throughout the test. This corresponds to the occurrence of adhesion right from the beginning in MAM-dry case (see blue arrows Fig. 3). For MAM-lubricated case, the forces

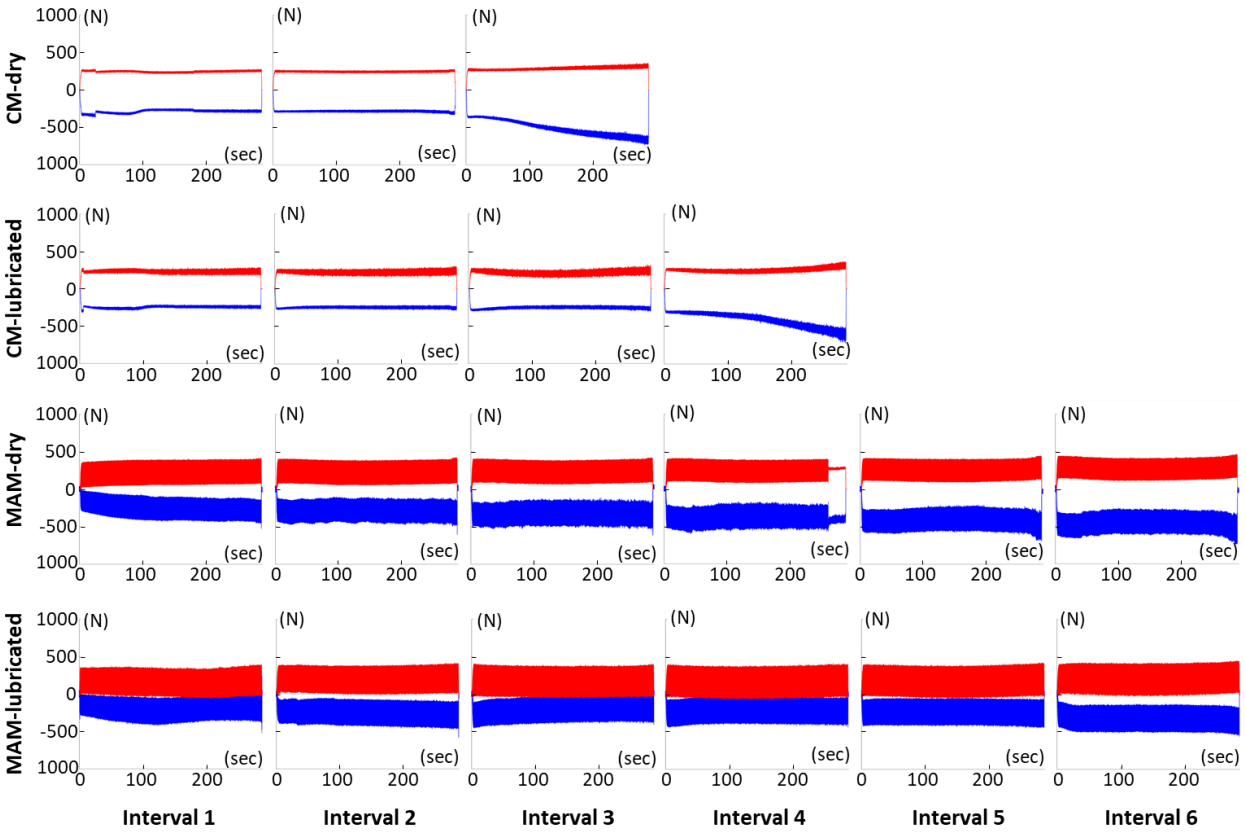

Figure 5. The time history of cutting force (red) and feed force (blue) during each cutting interval for the tools shown in Fig. 3.

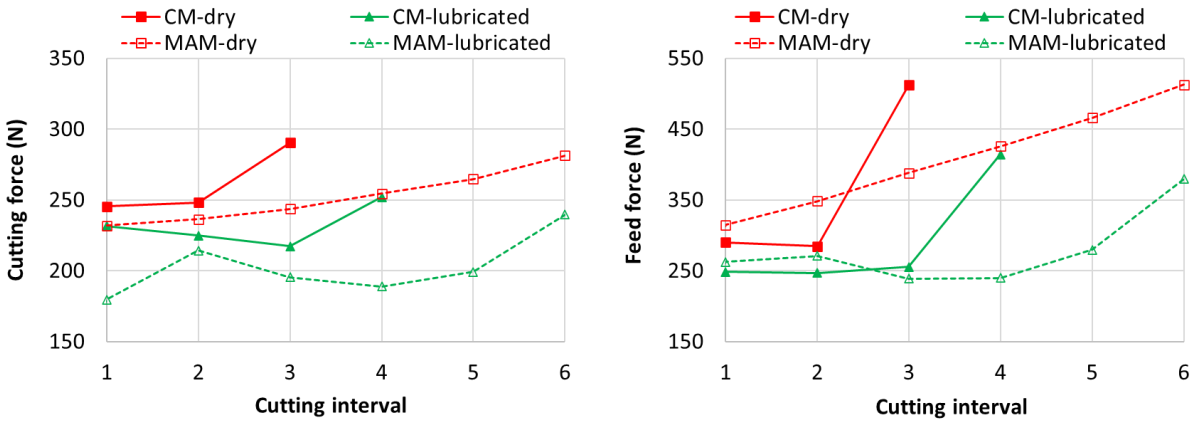

Figure 6. The averaged cutting force (a) and feed force (b) for each cutting interval corresponding to Fig. 5.

have similar trends as those in CM-dry and CM-lubricated cases. In other words, the forces do not change significantly before the occurrence of severe adhesion. The significant increase in forces in the last cutting interval corresponds to the rapid wear accompanied by severe adhesion. It is evident that the increase in the forces is mainly caused by tool adhesion in all the cases.

Figure 7 shows Keyence digital microscope images of the tools at the final cutting distance before and after etching for the four turning cases. Significant adhesion is clearly seen covering the tool flank in all cases. The adhesion is identified to be mainly iron (i.e., the work material) based on EDS analysis. The etched tool images reveal the actual tool wear in the adhesion region: the tool coating is completely breached, and the carbide substrate is exposed which is also confirmed by EDS analysis. Generally, the coating breached region matches well with the adhesion region. In both CM-dry and CM-lubricated cases, the breached region is primarily on the main flank and slightly extends to the nose flank. In MAM-lubricated case, the breached region is located continuously from the nose flank to the main flank. In MAM-dry case, the breached region is however separated on the nose flank and at the end of the main flank (i.e.,

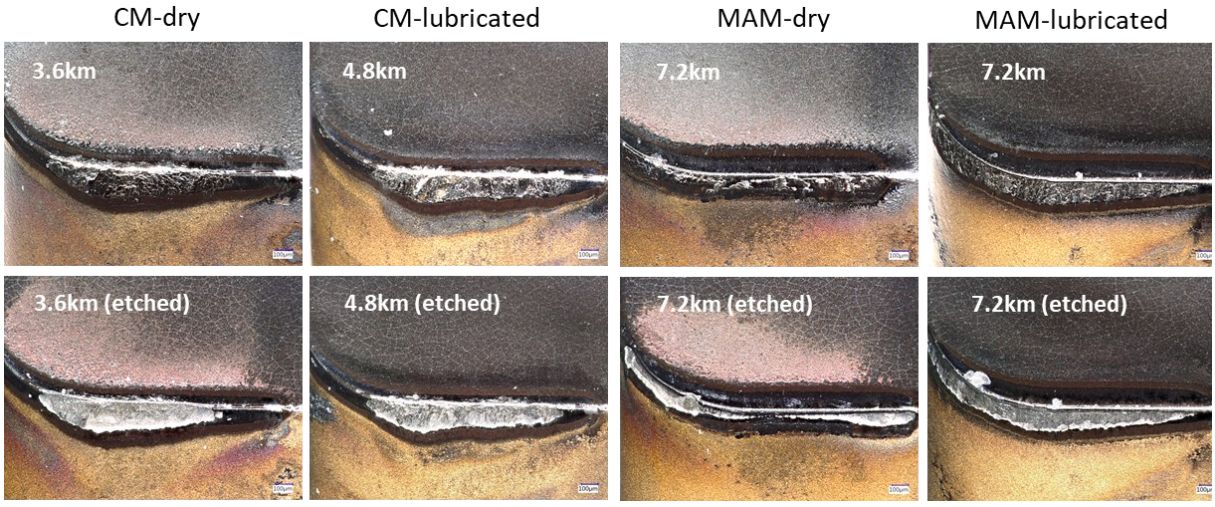

Figure 7. Unetched (top) and etched (bottom) tool images for each turning condition at the final cutting distance. Tool number: 1, 2, 3 and 4.

away from the nose); the coating in the middle of the main flank is barely breached as shown in Figure 7. The total breached area in MAM-dry case is the smallest among all cases. In addition, the breached region does not match with the adhesion region as clearly as in the other cases; the adhesion appears to also occur in the middle region of the main flank where coating has not been breached.

Figure 8 shows the tools after the first or second cutting intervals where coating has not been breached for the four cases. Some damages are observed on the cutting edge in both CM-dry and CM-lubricated cases (see red arrows). In contrast, no such damages occur on the cutting edge in MAM-dry and MAM-lubricated cases. Significant amount of adhesion is also observed on the tool flank in MAM-dry case (see yellow arrows) while the tool flank appears much cleaner in the other cases. This is consistent with the observations in Figure 3. It is now clear that there are two types of adhesion occurring in MAM-dry case: the adhesion on the coating and the adhesion on the exposed carbide once the coating is breached. For the other cases, the adhesion only occurs on the exposed carbide after coating is breached. In other words, the initiation of adhesion does not occur until the coating on the tool is breached.

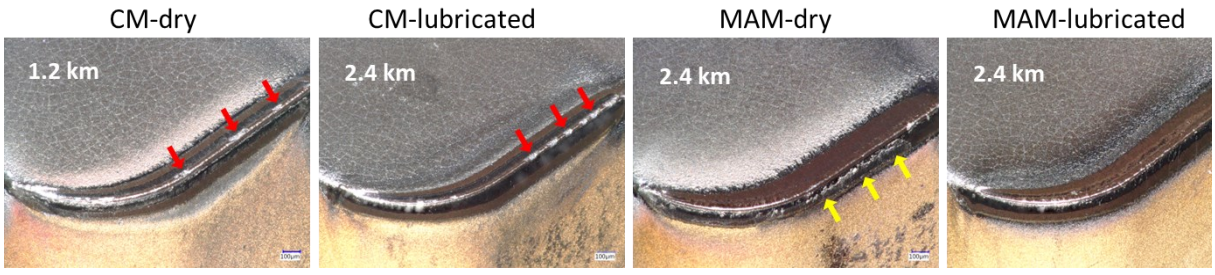

Figure 8. Unetched tool images for each turning condition before tool coating is breached. Tool number: 5, 6, 7 and 8.

4.2. Wear characteristics in dry condition

Figure 9 shows detailed comparison of the tools after etching in CM-dry and MAM-dry cases. There are several notable distinctions. First, in CM-dry case, coating breach occurs very early (at the cutting distance of 2.4 km). The breach on the tool flank starts in the middle region along the cutting edge (Fig. 9a) and grows rapidly on the main flank along the side cutting edge (Fig. 9b). In MAM-dry case, coating breach starts from two ends of the tool flank. i.e., the nose flank and the end of the main flank (Fig. 9d). The expansion of the two breached zones into the middle region is quite slow. At the cutting distance of 7.2 km (Fig. 9e), the breached zone in the middle region only appears as a barely connected slit running parallel to the cutting edge at the center of the wear land. Secondly, in CM-dry case, the breached zone extends over the cutting edge. The cutting edge outside the breached zone also shows many damages as micro-chipping

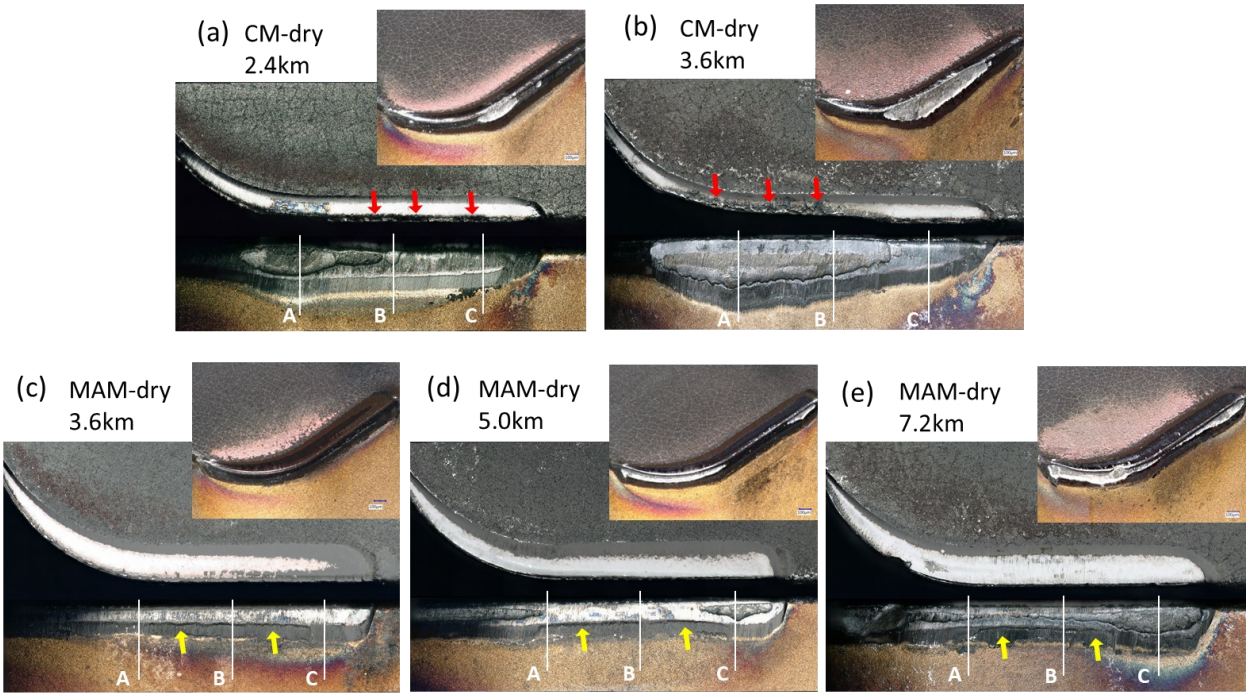

Figure 9. Digital microscope images of etched tools with different cutting distances in CM-dry (top row) and MAM-dry (bottom row) turning tests. Tool number: 5, 1, 9 10 and 3.

(red arrows in Fig. 9a). Furthermore, the rake face next to the breached cutting edge shows the burned colors indicating a higher temperature in this region. As the breached zone further increases in size, the rake face coating near the breached edge also shows many damages leading to a very rough rake face (red arrows in Fig. 9b). In MAM-dry case, coating breach is limited only on the flank face. The breach does not extend to the cutting edge. The cutting edge remains well preserved without any chipping damages both before and after the coating is breached on the flank face. The rake face coating is also preserved well. The rake face shows no burned colors and appears very smooth. Thirdly, in MAM-dry case, a thick layer of material which forms a noticeable geometric step on the flank wear land can be observed at all cutting distances (see yellow arrows in Fig. 9c-e). The same layer and step cannot be clearly observed on the tools in CM-dry case.

Figure 10 shows the section profiles of the flank wear lands of the etched tools shown in Figure 9. For each tool, the gray, orange, and blue profiles are corresponding to the section locations A, B, and C marked in Figure 9, respectively. These profiles further confirm the

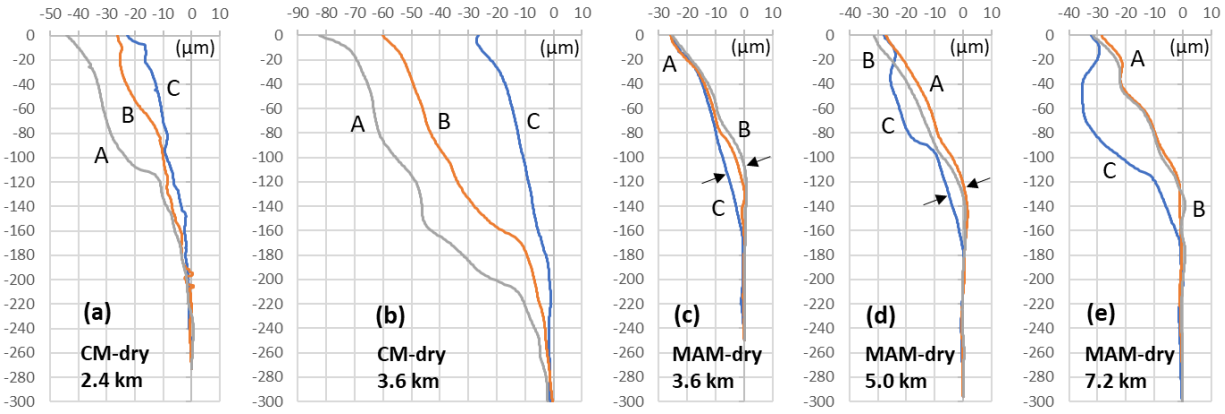

Figure 10. Section profiles of the flank wear lands of the etched tools shown in Fig. 9. The three section planes (A, B and C) for each tool are marked in Fig. 9. The gray, orange, and blue profiles correspond to sections A, B, and C, respectively.

significantly different wear characteristics in CM-dry and MAM-dry cases. In CM-dry case, both the height and depth of the flank wear (measured in directions parallel and perpendicular to the flank face respectively) are increased rapidly and become substantially high after the coating is breached (Fig. 10a and 10b). The maximum flank wear depth is seen always at the cutting edge (the top side of the curve). In contrast, in MAM-dry case, both the height and depth of the flank wear increase at a much lower rate. Note the drastic difference in the profiles between CM-dry and MAM-dry cases after cutting the same distance of 3.6 km (Fig. 10b and 10c). In MAM-dry case, the profiles at the coating breached zone show a concave shape or valley below the cutting edge (see blue profiles in Fig. 10d and 10e). This again indicates the breach does not occur at the cutting edge. At the cutting distance of 7.2 km, the maximum flank wear depth is no longer at the cutting edge but at the valley of the breached zone (see blue profile in Fig. 10e). The flank wear depth at the cutting edge increases very slowly in MAM-dry case, i.e., increasing only from ~ 25 μm to ~ 30 μm when cutting distance is increased from 3.6 km to 7.2 km (Fig. 10c-e). In contrast, in CM-dry case, this depth value increases from ~ 25 μm up to ~ 80 μm when cutting distance is only increased from 2.4 km to 3.6 km (Fig. 10a and 10b).

Furthermore, the distinctive layer and step observed on the flank wear land in MAM-dry case (yellow arrows in Fig. 9c-e) are also noted on the corresponding profiles (Fig. 10c-e). For example, in Fig. 10c, the gray and orange profiles show a convex shape between -80 μm and -160 μm in y-axis where the blue profile remains straight. This is because the layer exists at section location A and B but not at location C (Fig. 9c). Similar observations can be made on the profiles in Fig. 10d and 10e approximately between -100 μm and -180 μm in y-axis, but not on profiles in Fig. 10a and 10b which are for CM-dry case. In addition, by comparing the gray and

orange profiles with the blue profile in Fig. 10c and 10d (see the arrows), the layer thickness may be estimated at about 10 μm.

Figure 11 shows the EDS analysis on the flank wear land for the same tools in Figure 9. For the spectrum at each marked location, only elements with atomic percent higher than 5% are displayed. Spectra 1 and 5 (gray) indicate the iron adhesion that has not been completely removed by etching; spectra 2, 4 and 10 (orange) indicate the exposed carbide substrate; spectra 3, 6, 9 and 13 (blue) indicate the exposed Al_2O_3 coating; spectra 7 and 11 (yellow) indicate the exposed Tic coating; spectra 8 and 12 (green) indicate the silicon oxide (SiO_2) deposition layer (based on the presence of Si and O) which cannot be etched by HCl acid. It is evident the SiO_2 layer is formed in MAM-dry case but not in CM-dry case. The SiO_2 layer seems to be mainly formed on the exposed Al_2O_3 coating layer. Before coating breach occurs (3.6 km), the SiO_2 layer is present on both the nose flank and the main flank except at the end of the cutting edge.

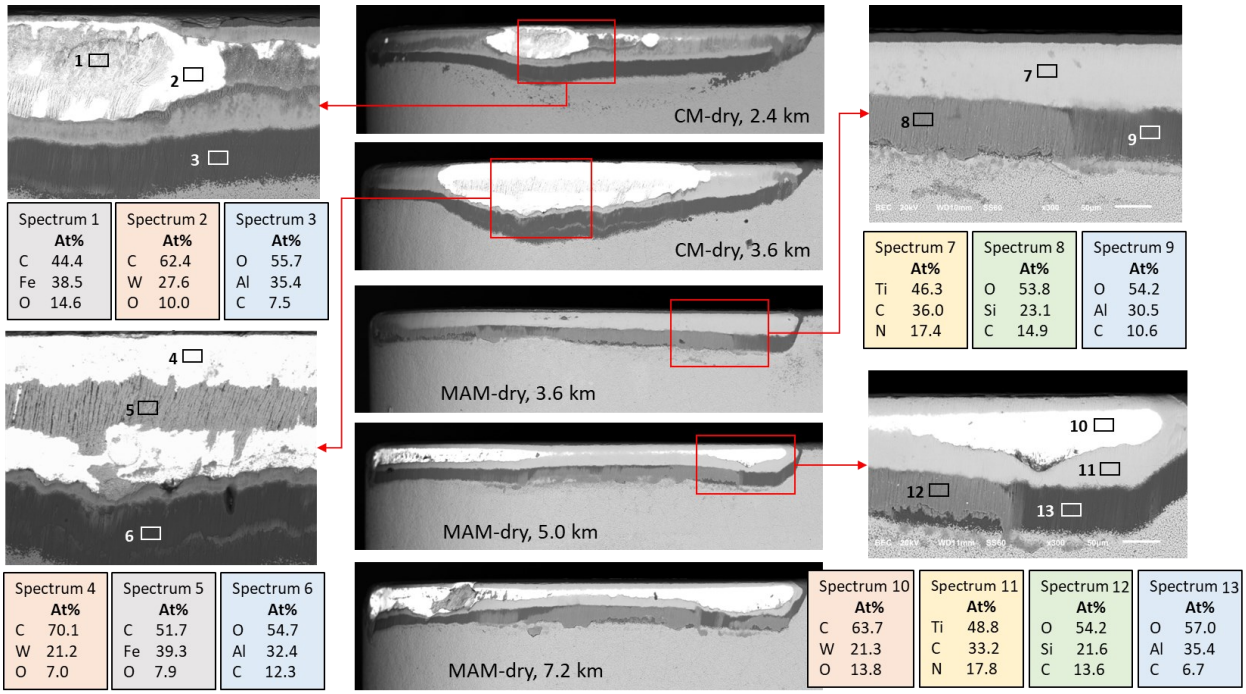

Figure 11. EDS analysis of the flank wear land of the etched tools in Fig. 9.

After coating is breached (5.0 and 7.2 km), the SiO_2 layer is still present on the main flank. It is evident there is significantly less wear in the corresponding flank region where SiO_2 layer is present.

4.3. Wear reduction mechanisms

The effect of SiO_2 layer formation can be illustrated in Figure 12. When there is no such layer formation in CM-dry case (Fig. 12a), the iron work material will not adhere to the flank wear land until the coating is breached. The coating on the flank is directly subjected to the intense rubbing by the newly generated work surface leading to higher rate of abrasive wear. In contrast, in MAM-dry case (Fig. 12b), a stable SiO_2 deposition layer is formed on the trailing edge of the flank wear land where Al_2O_3 coating is exposed. The SiO_2 layer is thick enough to create a geometrical step on the flank wear land. This will result in the accumulation of stagnated iron in front of the step covering the upper portion of the wear land where the Tic coating is exposed (Fig. 12b). The stagnated iron layer accumulated by the SiO_2 deposition layer protects the flank coating from the intense rubbing by the newly generated work surface. Therefore, the abrasive wear on the flank coating is significantly reduced. The unique adhesion previously

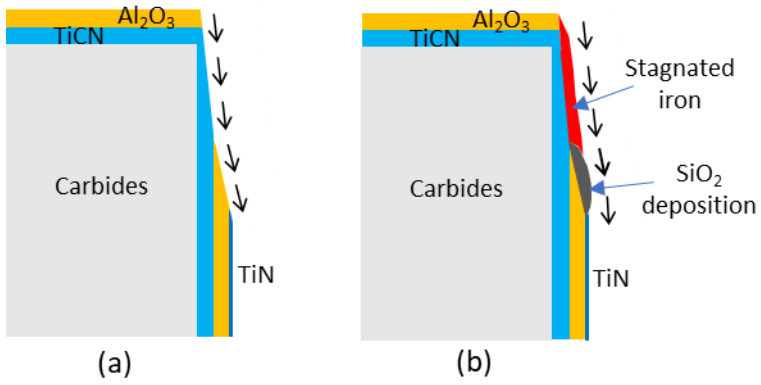

Figure 12. Schematic illustration of the tribological condition at the tool flank in (a) CM-dry and (b) MAM-dry case.

observed on the tool coating in MAM-dry case (see Figs. 3, 7 and 8) is in fact the stagnated iron which is formed purely due to the geometric effect created by the presence of the SiO_2 deposition layer. Like iron adhesion (on exposed carbide), the stagnated iron will increase the cutting forces (see Figs. 5 and 6), but unlike iron adhesion, the stagnated iron will greatly reduce the flank wear (see Fig. 4).

Besides the formation of SiO_2 layer and stagnated iron, the ability to preserve the coating on the cutting edge (rake side) is another important factor which leads to the wear reduction in MAM-dry case. In CM-dry case, the coating at the cutting edge is not well preserved. Damages on edge coating occur even before the breach of coating on the flank. After the coating is breached on the flank, coating damages on the cutting edge exacerbate the rapid wear on the flank which is illustrated in Fig. 13a. When the coating AB is damaged and broken away, severe iron adhesion will occur on the exposed carbide around the edge BAA'. Considering the material flow direction (V_c), the wear on the exposed carbide will progress rapidly changing the flank profile from AA' to BB' and the cutting edge moving from A to B. Coating BC is again broken away which will allow flank wear to progress rapidly from BB' to CC'. Similarly, when coating CD is broken away, flank wear will progress rapidly from CC' to DD'. Note the breaking of edge coating at the rake side and the progression of flank wear on the exposed carbide at the flank side occur simultaneously in this process through the iron adhesion layer.

In MAM-dry case, the coating at the cutting edge is well preserved even after the coating is breached on the flank. This slows down the rapid wear on the exposed carbide on the flank side which is illustrated in Fig. 13b and 13c. Since the edge coating on the rake side is well preserved, severe adhesion can only occur on the flank side below the cutting edge where carbide is exposed (AA'). In this case, the wear will create a concave shaped profile or a valley on the

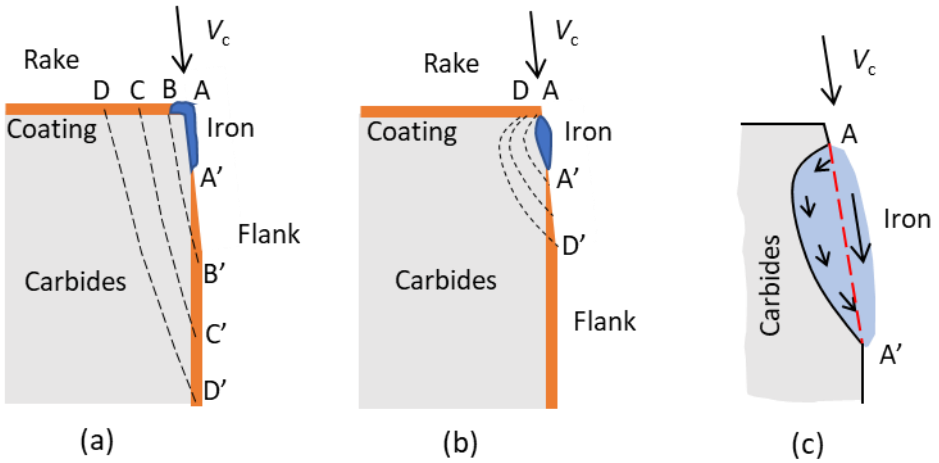

Figure 13. Schematic illustration of wear progression after coating breach in (a) CM-dry and (b, c) MAM-dry cases.

exposed carbide. Work material trapped inside the valley will flow at a lower velocity compared to the material outside the valley (Fig. 13c). This will reduce the shear intensity at the carbide interface and hence slow down the wear on the carbide. The deeper the created valley, the slower the material flow along the carbide interface, and hence the lower the wear rate on the carbide. This means the wear on the exposed carbide will decelerate. Eventually, the abrasive wear on the edge coating from the flank side will control the overall flank wear progression in the depth direction. Therefore, the flank wear depth is significantly smaller in MAM-dry case than CM-dry case (see Fig. 10).

4.4. Wear characteristics in lubricated condition

Figure 14 shows the spread of adhesion on tool flank in CM-lubricated and MAM-lubricated cases, which reflects the progression of coating breach. In CM-lubricated case, coating breach starts at a spot on the main flank which is close to the nose (see arrow in Fig. 12a). Then it quickly spreads to the main flank along the side cutting edge but does not progress to the nose flank (Fig. 12b). In MAM-lubricated case, the coating breach starts on the nose flank (see arrows in Fig. 12d) and then spreads to the main flank along the side cutting edge (Fig. 12e). The

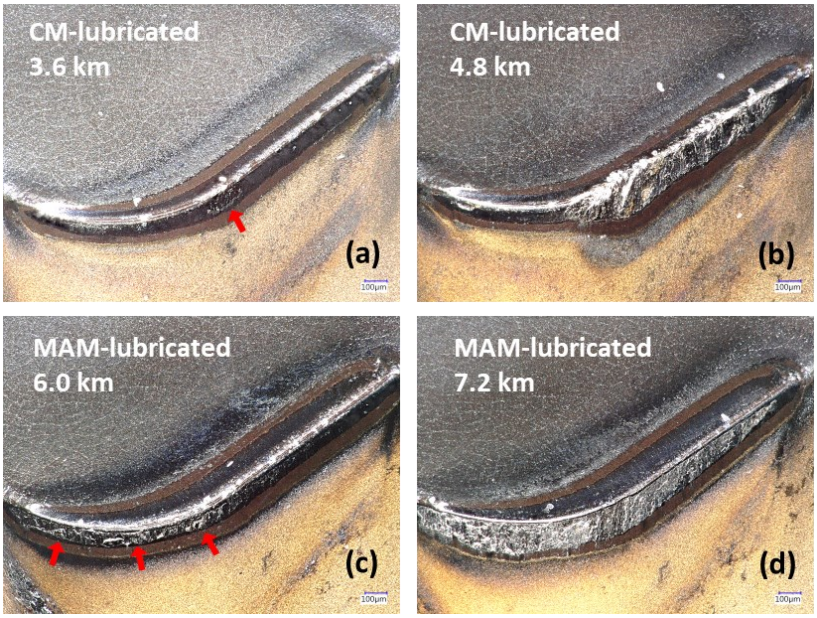

Figure 14. Digital microscope images of the tool edges at the last two cutting intervals in CM-lubricated (top row) and MAM-lubricated (bottom row) cases. Tool number: 2 and 4.

breaching process in CM-lubricated case is essentially the same as in CM-dry case. The breaching process in MAM-lubricated case is different from the MAM-dry case. There is no separate start of the breach at the end of the main flank, and the breached zone spreads from the nose flank to the main flank much faster than in CM-dry case.

Figure 15 shows the detailed comparison of the tools after etching in CM-lubricated and MAM-lubricated cases. Figure 16 shows the section profiles of the flank wear lands corresponding to the sections A, B and C marked in Figure 15. Figure 17 shows the EDS analysis of the marked tool flank region in Figs. 15a and 15c. It is evident the application of cutting fluid does not fundamentally alter the wear characteristics in CM turning. In CM-lubricated case, cutting edge is not well preserved as in CM-dry case; edge damages can be observed before the coating is breached on tool flank (see red arrows in Figs. 15a and 17a). Once the coating breach starts on tool flank, the unpreserved cutting edge exacerbates the rapid wear on the exposed carbide in the same way as illustrated in Fig. 13a. This is evidenced by the severe

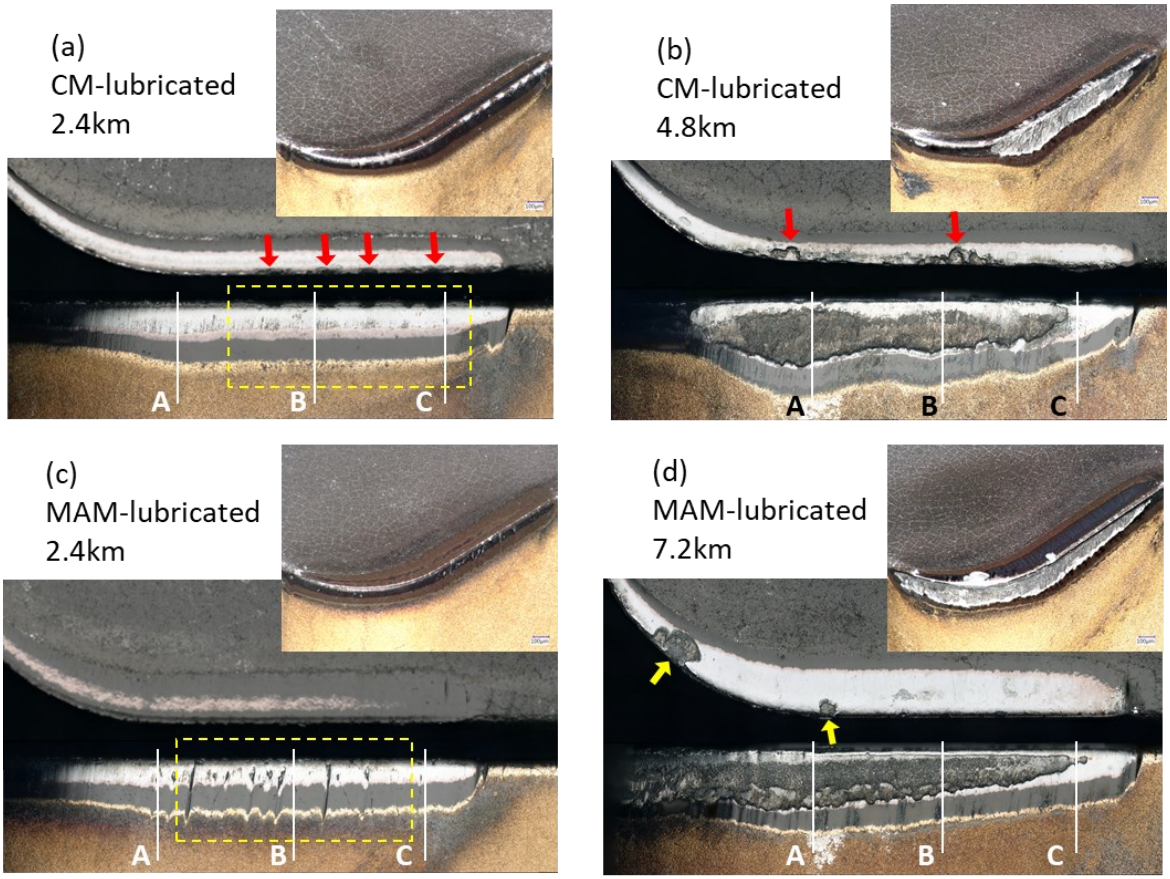

Figure 15. Digital microscope images of etched tools with different cutting distances in CM-lubricated (top row) and MAM-lubricated (bottom row) turning tests. Tool number: 6, 2, 8 and 4.

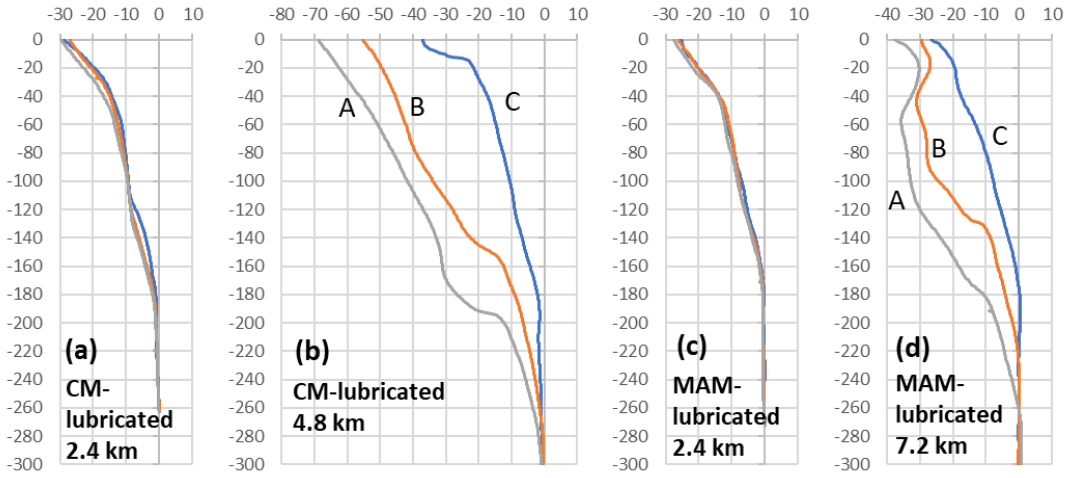

Figure 16. Section profiles of the flank wear lands of the etched tools shown in Fig. 15. The gray, orange, and blue profiles correspond to sections A, B, and C marked in Fig. 15, respectively.

coating damages on the rake side of the cutting edge (see red arrows in Fig. 15b), the substantially large height and depth of the flank wear (Fig. 16b), and especially the occurrence of maximum flank wear depth at the cutting edge (Fig. 16b). The cutting fluid does have some lubrication and cooling effects which can be inferred from the reduced forces (Fig. 6) and less burned color present on the tool rake face (Fig 15b compared to Fig. 9b). However, these effects are not dominant as they only result in slight improvement in tool life (Figs. 3 and 4).

The cutting fluid results in more fundamental changes on the wear characteristics in MAM turning. The SiO_2 layer, a geometric step on the flank, in MAM-dry case (Figs. 9c-9e and 10c) could not be observed in MAM-lubricated case (Figs. 15c, 15d and 16c). The EDS analysis also confirms there is no detection of SiO_2 on the flank in MAM-lubricated case (Fig. 17b). Apparently, the formation of the SiO_2 layer on the flank is precluded by the cutting fluid. Without the SiO_2 layer formation, there is no stagnated iron layer formation. Therefore, the wear

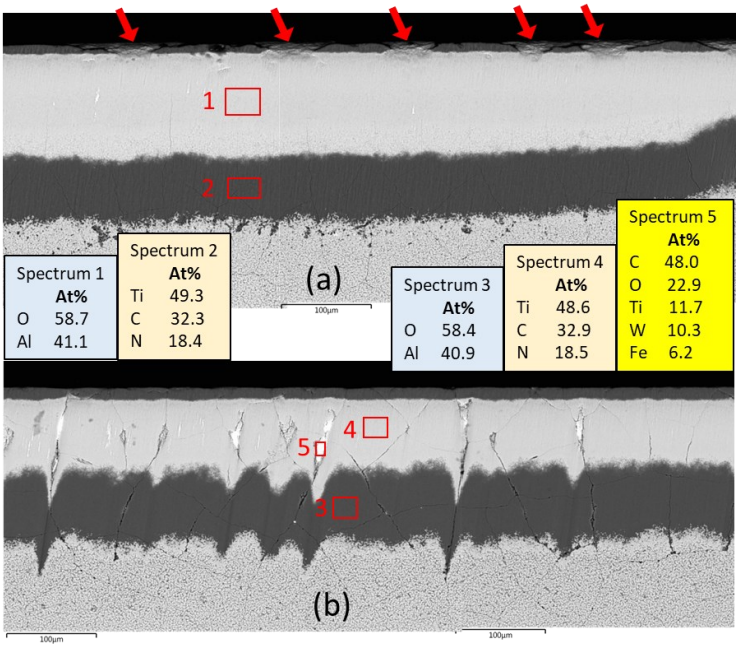

Figure 17. EDS analysis of the tool flank (after etching) at the cutting distance of 2.4 km in (a) CM-lubricated and (b) MAM-lubricated cases, corresponding to the marked region in Fig. 15a and 15c, respectively. Tool number: 6 and 8.

reduction mechanism illustrated in Fig. 12b does not occur in MAM-lubricated case. However, the wear reduction (compared to CM) due to the preservation of tool edge coating (see Fig. 13b and 13c) remains effective. This is evidenced by the smooth cutting edge and rake face in Figure 15d and the concave shaped flank profiles in Figure 16d. Note the two isolated coating damages on the rake face (yellow arrows in Fig. 15d) could not be observed until the tool is etched (see Fig. 14d). When comparing the flank wear between MAM-lubricated and MAM-dry cases, despite of the similar flank wear depth (~ 35 μm), the flank wear land is significantly lower in MAM-dry case (see Figs. 4, 10e and 16d). This indicates the preservation of tool edge coating is responsible for reducing flank wear depth and the SiO_2 layer formation is responsible for reducing the size of flank wear land.

The cutting fluid should have enhanced lubrication and cooling effects in MAM compared to CM turning, because the periodic disruptions at the tool-chip and tool-work interfaces allow the fluid to better access to the contact interfaces. However, the fluid also leads to larger temperature variation during MAM turning which tends to promote thermal cracking on the tool coating. These cracks can be clearly observed in Figure 17b. It is also evident when the coating cracks are large enough, they can trap the work material during cutting, which increases the local wear rate. Therefore, there are local variations in flank wear height and the wear land shows many pits and grooves (see Figs. 15c and 17b). However, the thermal cracks are not dominant on the overall wear progression as the effect remains local. It is the coating breach starting at the nose flank and quickly spreading to the main flank (see Figs. 14c, 14d and 15d) that is most influential on the final tool life in MAM-lubricated turning. In addition, thermal cracks are likely responsible for formation of the two coating damages while etching the tool as shown in Fig. 15d.

4.5. Coating breach in MAM turning

In both MAM-dry and MAM-lubricated cases, it is observed that the coating breach starts at the nose flank. This can be explained by the continuous contact and increased rubbing at the end cutting edge. Figure 18 shows the tool-work engagement in MAM turning where the effective cutting edge is marked as ABC. Due to the feed-direction modulation, the side cutting edge AB is periodically disengaged from the work material, but the end cutting edge at C always remains in contact with the cut work surface because the modulation is in the tangential direction of the contact at C. Moreover, the modulation results in additional rubbing at the end cutting edge. Therefore, a higher flank wear and a start of coating breach should be expected at the nose flank in MAM turning. In MAM-dry case, the spread of coating breach from the nose flank to the main flank occurs very gradually showing no apparent acceleration in wear progression. This should be attributed to the SiO_2 layer (and stagnated iron layer) protection. The coating breach emanated from the other end of the main flank is more likely due to the lack of SiO_2 layer protection (see Fig. 11). In MAM-lubricated case, coating breach only starts at the nose flank. Once the breach starts, it spreads quickly to the main flank showing an acceleration of the wear progression. This indicates that the cutting fluid is not as effective as the formation of SiO_2 layer in suppressing the spread of the breach. However, the cutting fluid is effective in reducing the

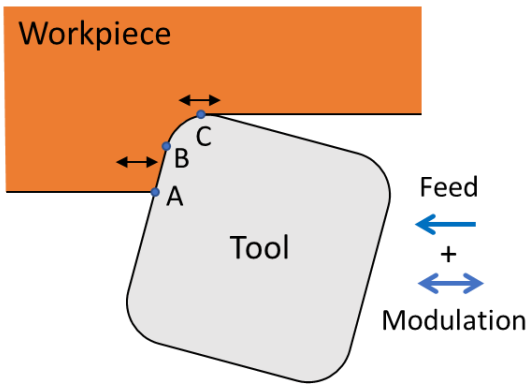

Figure 18. The tool-work engagement in MAM turning.

abrasive wear on the coating. This is evidenced by the significant reduction in wear at the end of the main flank compared to MAM-dry case (Fig. 15d vs. Fig. 9e). Note there is no SiO_2 layer protection at the end of the main flank for both cases, so the wear reduction in this region can be attributed only to the cutting fluid effect.

4.6. Further discussions

The success of MAM-dry case comes from the formation of SiO_2 layer which should be dependent on temperature, material, and the tool-work contact condition. The cutting speed and modulation frequency will likely influence this layer formation as they will change cutting temperature and tool-work contact disruptions. The tool coating material should also play an important role in this layer formation. The stable SiO_2 layer is found to mainly form on the exposed Al_2O_3 coating. This might be due to the strong adhesion between the two materials at the high temperature during cutting. Whether the same SiO_2 layer formation will occur on other types of coated tools, especially those without Al_2O_3 coating layer, will need further investigation. The SiO_2 layer formation apparently will depend on the work material. Besides CGI, the deposition layer may be formed in MAM-dry cutting of flake graphite iron (FGI), nodular graphite iron (NGI), and electrical steel which all have high silicon content. If so, significant tool wear reduction could also be achieved in cutting these materials by MAM. This is to be confirmed in future study.

The EDS analysis showed a fair amount of carbon present in the deposition layer (see Spectra 8 and 12 in Fig. 11). Due to the uncertainty in detecting carbon content by EDS analysis, the deposition layer so far has been identified as silicon oxide SiO_2. However, it is also possible that the formed deposition layer is silicon oxycarbide (SiOC) which has enhanced mechanical and electrical properties compared to silicon oxide (SiO_2) [30]. It has been shown that Al_2O_3 is a

good substrate material for fabricating SiOC-based thin films and coatings [31], which may explain the formation of the deposition layer preferably on the exposed Al_2O_3 coating.

The excellent preservation of the cutting tool edge (coating) during cutting is a common phenomenon in both MAM-dry and MAM-lubricated cases that contributes to the wear reduction compared to CM turning. Therefore, this phenomenon must be enabled by the unique cutting kinematics of MAM. The tool edge damages in CM turning are likely caused by the formation of build-up edge (BUE). Compared to FGI, the more ductile CGI and NGI have higher tendency to form BUE in a wider range of cutting speeds [13]. The repeated detaching and reforming of the BUE on the tool edge during cutting will likely cause the edge chipping and damages. It is possible that MAM can mitigate or suppress the formation of BUE due to the periodic disruptions at the tool-chip contact. Therefore, the tool edge is better preserved during MAM turning, which ultimately improve the machinability.

In the present study, the overall wear reduction in MAM-dry case (compared to CM) is more significant than that in MAM-lubricated case. Further study will be needed for more comprehensive evaluation in a wider range of cutting conditions (speed, federate, modulation frequency, fluid type, etc.). The key to the success of MAM-lubricated case is to control the wear at the nose flank due to the continuous contact and increased rubbing. The modulation frequency and amplitude and the tool nose radius will likely influence this wear. The cutting fluid used in the present study is simple vegetable oil which has more lubrication effect than the cooling effect. It is also worth testing water-based coolant in MAM. This will help determine the relative importance between the lubrication effect and cooling effect on the wear reduction. However, with water-based coolant, thermal cracking may become a potential issue, so a tradeoff between enhanced cooling and thermal cracking is likely needed.

5. Conclusions

In this study, the characteristics of tool wear evolution and cutting forces in conventional (CM) turning and modulated (MAM) turning of CGI with coated carbide tools are investigated at the cutting speed of 250 m/min. The following conclusions may be drawn from the study.

1. In CM turning, the coating breach on the main flank occurs very early triggering rapid wear on the exposed carbide accompanied by severe iron adhesion. The application of cutting fluid only slightly delays the breach of tool coating but cannot slow down the rapid wear and severe tool adhesion once coating is breached.
2. MAM can significantly reduce the tool wear compared to CM in both dry and lubricated cutting conditions. When comparing between MAM-dry and MAM-lubricated cases, the cutting forces are lower in MAM-lubricated case with the increase in the tool wear compared to MAM-dry case.
3. In MAM-dry case, two mechanisms account for the wear reduction: (1) the formation of SiO_2 deposition (and stagnated iron) protective layer on the tool flank face; and (2) the preservation of coatings on the tool cutting edge. The first mechanism is responsible for greatly reducing the flank wear land size while the second mechanism is responsible for greatly reducing the flank wear depth after the coating is breached.
4. In MAM-lubricated case, the cutting fluid precludes the formation of SiO_2 deposition layer. The wear reduction mechanisms (compared to CM) are changed to (1) the enhanced lubrication and cooling at periodically disrupted tool-chip and tool-work contacts and (2) the preservation of coatings on the tool cutting edge.
5. The start of coating breach at tool nose flank in MAM is due to the continuous contact and increase rubbing at the nose flank. The formation of SiO_2 deposition layer is more

effective than the cutting fluid to suppress the spread of coating breach from the nose flank to the main flank.

Acknowledgement

This work was supported by National Science Foundation (Grant number: 2019320). We thank Ryan Khawarizmi for the assistance in etching some of the cutting tools.

References

[1] Dawson SinterCast S. Compacted Graphite Iron-A Material Solution for Modern Diesel Engine Cylinder Blocks and Heads. 68th WFC-World Foundry Congr., 2008, p. 93–9.

[2] Stephenson DA, Agapiou JS. Metal cutting theory and practice, Third edition. 2016. https://doi.org/10.1201/b19559.

[3] Dawson S, Hollinger I, Robbins M, Daeth J, Reuter U, Schulz H. The Effect of Metallurgical Variables on the Machinability of Compacted Graphite Iron. SAE Tech. Pap., 2001. https://doi.org/10.4271/2001-01-0409.

[4] Abele E, Sahm A, Schulz H. Wear mechanism when machining compacted graphite iron. CIRP Ann - Manuf Technol 2002;51. https://doi.org/10.1016/S0007-8506(07)61464-4.

[5] Tooptong S, Park K-H, Kwon P. A comparative investigation on flank wear when turning three cast irons. Tribol Int 2018;120:127–39.

https://doi.org/10.1016/j.triboint.2017.12.025.

[6] Gastel M, Konetschny C, Reuter U, Fasel C, Schulz H, Riedel R, et al. Investigation of the wear mechanism of cubic boron nitride tools used for the machining of compacted graphite iron and grey cast iron. Int J Refract Met Hard Mater 2000;18:287–96.

[7] Heck M, Ortner HM, Flege S, Reuter U, Ensinger W. Analytical investigations concerning the wear behaviour of cutting tools used for the machining of compacted graphite iron and grey cast iron. Int J Refract Met Hard Mater 2008;26:197–206. https://doi.org/10.1016/j.ijrmhm.2007.05.003.

[8] Nguyen D, Tooptong S, Park KH, Kwon P. Formation mechanism of alumina layer in protecting cubic boron nitride inserts in turning cast irons. Int J Mach Tools Manuf 2020;153. https://doi.org/10.1016/j.ijmachtools.2020.103539.

[9] Da Silva MB, Naves VTG, De Melo JDB, De Andrade CLF, Guesser WL. Analysis of wear of cemented carbide cutting tools during milling operation of gray iron and compacted graphite iron. Wear 2011;271:2426–32. https://doi.org/10.1016/j.wear.2010.11.030.

[10] de Sousa JAG, Sales WF, Machado AR. A review on the machining of cast irons. Int J Adv Manuf Technol 2018;94:4073–92. https://doi.org/10.1007/s00170-017-1140-1.

[11] Mocellin F, Melleras E, Guesser WL, Boehs L. Study of the Machinability of Compacted Graphite Iron for Drilling Process. J Brazilian Soc Mech Sci Eng 2004;26. https://doi.org/10.1590/S1678-58782004000100004.

[12] Tasdelen1, B. M. Escursell, G. Grenmyr Nyborg L. Machining of gray cast irons and

compacted graphite iron. Swedish Prod Symp 2007.

[13] Dearnley PA. A metallurgical evaluation of tool wear and chip formation when machining pearlitic grey cast irons with dissimilar graphite morphologies. Wear 1985;101:33–68. https://doi.org/10.1016/0043-1648(85)90210-8.

[14] Childs T, Maekawa K, Obikawa T, Yamane Y. Metal machining–theory and applications, 2000. Arnold, London 2000.

[15] Nayyar V, Kaminski J, Kinnander A, Nyborg L. An Experimental Investigation of Machinability of Graphitic Cast Iron Grades; Flake, Compacted and Spheroidal Graphite Iron in Continuous Machining Operations. Procedia CIRP 2012;1:488–93. https://doi.org/10.1016/J.PROCIR.2012.04.087.

[16] Shokrani A, Dhokia V, Newman ST. Environmentally conscious machining of difficult-to-machine materials with regard to cutting fluids. Int J Mach Tools Manuf 2012;57. https://doi.org/10.1016/j.ijmachtools.2012.02.002.

[17] Melkote S, Kumar M, Hashimoto F, Lahoti G. Laser assisted micro-milling of hard-to-machine materials. CIRP Ann - Manuf Technol 2009;58. https://doi.org/10.1016/j.cirp.2009.03.053.

[18] Skvarenina S, Shin YC. Laser-assisted machining of compacted graphite iron. Int J Mach Tools Manuf 2006;46:7–17. https://doi.org/10.1016/j.ijmachtools.2005.04.013.

[19] Moriwaki T, Shamoto E. Ultraprecision Diamond Turning of Stainless Steel by Applying Ultrasonic Vibration. CIRP Ann - Manuf Technol 1991;40. https://doi.org/10.1016/S0007-8506(07)62053-8.

[20] Shamoto E, Moriwaki T. Study on Elliptical Vibration Cutting. CIRP Ann - Manuf Technol 1994;43. https://doi.org/10.1016/S0007-8506(07)62158-1.

[21] Brehl DE, Dow TA. Review of vibration-assisted machining. Precis Eng 2008;32. https://doi.org/10.1016/j.precisioneng.2007.08.003.

[22] Mann JB, Guo Y, Saldana C, Compton WD, Chandrasekar S. Enhancing material removal processes using modulation-assisted machining. Tribol Int 2011;44:1225–35.

[23] Sui H, Zhang X, Zhang D, Jiang X, Wu R. Feasibility study of high-speed ultrasonic vibration cutting titanium alloy. J Mater Process Technol 2017;247. https://doi.org/10.1016/j.jmatprotec.2017.03.017.

[24] Guo Y, Stalbaum T, Mann J, Yeung H, Chandrasekar S. Modulation-assisted high speed machining of compacted graphite iron (CGI). J Manuf Process 2013;15. https://doi.org/10.1016/j.jmapro.2013.06.001.

[25] Sandoval J, Ali A, Kwon P, Guo Y. Modulation-assisted machining of compacted graphite iron with coated carbide tool in dry condition. Manuf Lett 2022;33:452–60. https://doi.org/10.1016/J.MFGLET.2022.07.058.

[26] Zhang D, Wang L. Investigation of chip in vibration drilling. Int J Mach Tools Manuf 1998;38:165–76. https://doi.org/10.1016/S0890-6955(97)00047-3.

[27] Guo Y, Mann JB. Control of chip formation and improved chip ejection in drilling with modulation-assisted machining. J Manuf Sci Eng Trans ASME 2020;142. https://doi.org/10.1115/1.4046829.

[28] Moscoso W, Olgun E, Compton WD, Chandrasekar S. Effect of Low-Frequency

Modulation on Lubrication of Chip-Tool Interface in Machining. J Tribol 2005;127:238–44. https://doi.org/10.1115/1.1829720.

[29] Yeung H, Sundaram NK, Mann JB, Dale Compton W, Chandrasekar S. Energy dissipation in modulation assisted machining. Int J Mach Tools Manuf 2013;74:41–9. https://doi.org/10.1016/J.IJMACHTOOLS.2013.07.007.

[30] Renlund GM, Prochazka S, Doremus RH. Silicon oxycarbide glasses: Part II. Structure and properties. J Mater Res 1991;6:2723–34. https://doi.org/10.1557/JMR.1991.2723.

[31] Stabler C, Ionescu E, Graczyk-Zajac M, Gonzalo-Juan I, Riedel R. Silicon oxycarbide glasses and glass-ceramics: "All-Rounder" materials for advanced structural and functional applications. J Am Ceram Soc 2018;101:4817–56. https://doi.org/10.1111/jace.15932.